Science of the Total Environment 866 (2023) 161439

Contents lists available at ScienceDirect

Science of the Total Environment

journal homepage: www.elsevier.com/locate/scitotenv

Loss of subsurface particulate and truly dissolved phosphorus during various flow conditions along a tile drain–ditch–brook continuum

Nina Siebers [a,*], Jens Kruse [a,b], Yunsheng Jia [a], Bernd Lennartz [c], Stefan Koch [c]

[a] Institute of Bio and Geosciences–Agrosphere (IBG-3), Forschungszentrum Jülich, D-52425 Jülich, Germany
[b] Institute of Crop Science and Resource Conservation (INRES), Soil Science and Soil Ecology, University of Bonn, Nussallee 13, 53115 Bonn, Germany
[c] Faculty of Agricultural and Environmental Sciences, University of Rostock, Justus-von-Liebig-Weg 6, D-18051 Rostock, Germany

HIGHLIGHTS

- Dissolved and colloidal P was monitored during discharge period to estimate P loss.
- Hierarchically (tile drain, ditch, brook) sampling during baseflow and event flow.
- AF^4 analyses revealed 33–34 % higher particulate P losses during event flow.
- Nanocolloids from C horizon are transported through tile drain into water.
- Event flow facilitates to transport of larger particles through soil matrix.

GRAPHICAL ABSTRACT

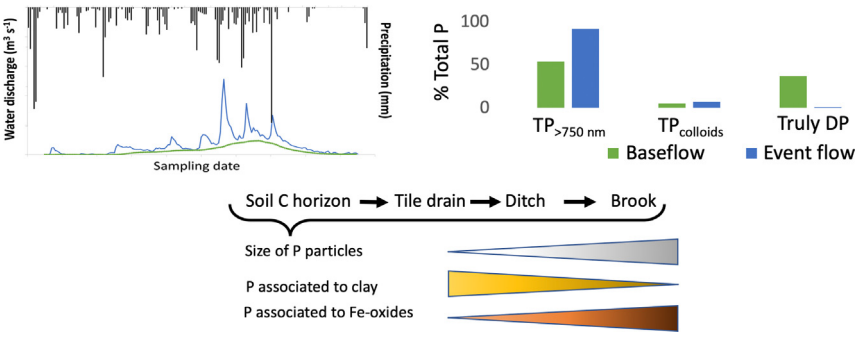

ARTICLE INFO

Editor: Frederic Coulon

Keywords:
Phosphorus leaching
Colloid transport
Flow component separation
Lowland catchment
Asymmetric flow field-flow fractionation

ABSTRACT

Subsurface losses of colloidal and truly dissolved phosphorus (P) from arable land can cause ecological damage to surface water. To gain deeper knowledge about subsurface particulate P transport from inland sources to brooks, we studied an artificially drained lowland catchment (1550 ha) in north-eastern Germany. We took daily samples during the winter discharge period 2019/2020 at different locations, i.e., a drain outlet, ditch, and brook, and analyzed them for total P ($TP_{unfiltered}$), particulate P >750 nm ($TP_{>750\ nm}$), colloidal P ($TP_{colloids}$), and truly dissolved P (truly DP) during baseflow conditions and high flow events. The majority of $TP_{unfiltered}$ in the tile drain, ditch, and brook was formed by $TP_{>750\ nm}$ (54 to 59 %), followed by truly DP (34 to 38 %) and a small contribution of $TP_{colloids}$ (5 to 6 %). During flow events, 63 to 66 % of $TP_{unfiltered}$ was present as particulate P ($TP_{>750\ nm}$ + $TP_{colloids}$), whereas during baseflow the figure was 97 to 99 %; thus, truly DP was almost negligible (1 to 3 % of $TP_{unfiltered}$) during baseflow. We also found that colloids transported in the water samples have their origin in the water-extractable nanocolloids (0.66 to 20 nm) within the C horizon, which are mainly composed of clay minerals. Along the flow path there is an agglomeration of P-bearing nanocolloids from the soil, with an increasing importance of iron(III) (hydr)oxides over clay particles. Event flow facilitated the transport of greater amounts of larger particles (>750 nm) through the soil matrix. However, the discharge did not exhaust colloid mobilization and colloidal P was exported through the tile-drainage system during the complete runoff period, even under baseflow conditions. Therefore, it is essential that the impact of rainfall intensity and pattern on particulate P discharge be considered more closely so that drainage management can be adjusted to achieve a reduced P export from agricultural land.

1. Introduction

Under the Helsinki Convention, numerous measures have been taken to reduce excessive nutrient inputs to the Baltic Sea. Although between 1995 and 2019 these measures reduced total phosphorus (P) and nitrogen

* Corresponding author.
E-mail address: n.siebers@fz-juelich.de (N. Siebers).

http://dx.doi.org/10.1016/j.scitotenv.2023.161439
Received 16 August 2022; Received in revised form 3 January 2023; Accepted 3 January 2023
Available online 6 January 2023

(N) inputs by ~35 % and ~19 % respectively (HELCOM, 2022), >97 % of the Baltic Sea still suffers from eutrophication due to historical and ongoing excessive nutrient inputs, which have an increasing effect on the Baltic Sea ecosystem (HELCOM, 2018a). P is of particular importance since it is the main regulating nutrient element for eutrophication in the Baltic Sea. It enters the Baltic Sea almost exclusively (~95 %) in waterborne form via riverine discharge (HELCOM, 2022). The main sources (~70 %) of waterborne P inputs are diffuse (agriculture, natural background, and storm overflows) and associated to a large degree with agricultural activity (HELCOM, 2018b). In Germany, for instance, agriculture accounts for around 51 % of P inputs, whereas P inputs from point sources (24 %) have been considerably reduced over the last few decades due to technical improvements in waste treatment plants and industry (HELCOM, 2018b; Nausch, 2011).

The subsurface transport of dissolved and particulate P from arable land by means of tile drains has been the subject of intensive research, because drains shorten the flow paths of water by bypassing large parts of the soil volume, which reduces the P retention potential of the soil and thus increases P losses (Nazari et al., 2022). For this reason, a program to monitor element emissions from soil to surface waters in the Zarnow River basin (north-eastern Germany, 49.5 km^2) was initiated in 2001 (Nausch et al., 2017). This program uses a hierarchical approach to estimate the transport of P from the tile drain to a ditch, a brook, and finally a stream (Bitschofsky and Nausch, 2019; Kahle, 2009; Nausch et al., 2017; Tiemeyer et al., 2006, 2009; Zimmer et al., 2016).

Both this monitoring program and recent literature revealed that dissolved P (DP) contributes to total P (TP) losses to a greater extent than previously acknowledged (Hahn et al., 2014; Jordan-Meille and Dorioz, 2004; Kleinman et al., 2007), with a contribution to total losses of between 16 and 69 % (Jiang et al., 2021; Nausch et al., 2017; Rodriguez et al., 2020; Ruark et al., 2012). However, there is considerable methodological uncertainty surrounding the determination of the DP fraction. For example, water samples collected as part of the Zarnow catchment monitoring program are treated with filters with a pore size between 0.4 and 0.8 μm, and P in 0.45 μm filtered samples is considered by definition as dissolved (Greenberg et al., 1985). However, the definition of natural colloids (1 to 1000 nm), as well as their subset natural nanoparticles (1 to 100 nm), overlaps with the definition of dissolved components (Jarvie et al., 2012). Hence, although DP is intended to be an estimate of the dissolved fraction only, it may in fact still contain large amounts of P bound to nanoparticles and colloids. Losses of P and other nutrients due to particulate transport are a rising concern (Bauke et al., 2022; Gottselig et al., 2017a, 2017b; Jiang et al., 2015, 2021). Major parts of soil P are bound within organic matter structures or tightly adsorbed to mineral particles (Alewell et al., 2020). In contrast, apart from soils excessively fertilized with P, only a small part of soil P is present in dissolved form (Helfenstein et al., 2018). Therefore, P losses from agricultural land to water bodies are mostly linked to particulate P of various size fractions that is mobilized during sudden rain events, either via surface runoff and soil erosion (nm to mm size range) or via subsurface transport due to internal soil erosion (nm to μm size range) (Carpenter and Bennett, 2011; Quinton et al., 2010).

Nanocolloids and fine colloids (<450 nm) in particular are more prone to leaching through the soil profile (Fresne et al., 2022); however, larger particles >450 nm can also be transported by means of macropore and preferential flow (McGechan and Lewis, 2002; Wang et al., 2020). Generally, natural colloids are increasingly being recognized as relevant carriers of nutrients in ecosystems due to their composition and high specific surface area (Burger et al., 2021; Gottselig et al., 2017a, 2017b; Hens and Merckx, 2002; Jiang et al., 2015, 2021). Fine colloids (<450 nm) are highly mobile in soils, and the colloid-facilitated transport of elements is highly dynamic as such transport is closely connected to water movement in the soil (Koch et al., 2016). Thus, losses of P and other nutrients due to particulate transport are a matter of growing concern (Gottselig et al., 2017a, 2017b; Jiang et al., 2015, 2021). It was shown that soil colloids in acidic freshwaters are associated with iron (Fe) and organic carbon (C_{org}) (Andersson et al., 2006; Neubauer et al., 2013) as well as clay minerals in the size range between 100 and 450 nm (Missong et al., 2018; Gottselig et al., 2017a). P preferentially binds to colloids composed of C_{org}, Fe/aluminum (Al) oxides, clay minerals, or calcium carbonates (Domagalski and Johnson, 2011; Gottselig et al., 2014, 2017a, 2017b; Gu et al., 2020; Jiang et al., 2015, 2021) mainly forming moderately labile Fe- and Al-associated P and non-labile hydroxyapatite (Liu et al., 2014).

One technique for analyzing both truly dissolved and colloidal elemental exports is asymmetric flow field-flow fractionation (AF^4), which enables the continuous high-resolution size separation of colloids (Baalousha et al., 2011; Qureshi and Kok, 2011). AF^4 is an elution technique in which a narrow sample band or pulse is injected into a stream of liquid and subjected to a field (i.e., crossflow) acting perpendicular to the stream. This leads to different particle retention times and thus to the separation of particles in the flow channel according to particle size. Therefore, particles of different sizes will exit the flow channel at different times, yielding specific elution profiles known as fractograms (Schimpf et al., 2000). The technique allows truly dissolved elements to be determined, as a permeable membrane is located at a site within the channel through which the liquid carrier solution, including all dissolved elements, constantly exits the channel. Therefore, AF^4 is perfectly suited to estimate the potential of subsurface P losses in both colloidal and truly dissolved forms.

Colloidal-bound P may partly explain elevated P concentrations in surface water during baseflow and especially during high flow conditions (Burger et al., 2021; Filella et al., 2006; Fresne et al., 2021; Jiang et al., 2021). As a consequence of climate change, Germany will experience more precipitation events in winter and less frequent, but more intense, precipitation events during the summer (Federal German Government, 2015). In Germany, the average precipitation levels in the winter season have increased by 25 % since winter 1881/1882 (German Environment Agency, 2019). Even though precipitation events are of longer duration and lower intensity in winter, winter events are predicted to create high colloidal peak discharges in streams and rivers. It was found that particle-facilitated transport of P dominates P transport in winter, reaching a maximum of 80 % of total P loss (Schelde et al., 2002). As not only the quantity varies with flow events but also the P speciation (Bender et al., 2018; Esbroeck et al., 2017), detailed knowledge about the subsurface transport of P in different forms (i.e., dissolved, colloidal, particulate) to adjacent surface waters is essential in order to optimize agricultural practices and reduce P losses. Therefore, the objective of this study was to explore the phosphorus export mechanism from tile-drained agricultural fields by analyzing particle size fractions in the discharge. In doing so, we aimed to (i) identify the extent to which precipitation patterns and intensity as well as discharge lead to the mobilization of particles of different sizes, (ii) compare particulate and dissolved losses, and (iii) determine the origin of particles transported by water in the adjacent field.

2. Materials and methods

2.1. Study site, sampling, and baseflow separation

The "Zarnow catchment" study site is located about 15 km southeast of the city of Rostock; the Zarnow brook is a tributary of the Warnow River. It is part of the Pleistocene lowland landscapes of north-eastern Germany and characterized by gentle slopes with maximum elevation differences of 30–50 m. It is a rural catchment typical of the federal state of Mecklenburg-Western Pomerania, and its primary land use is arable land (<60 %) (Nausch et al., 2017). The primary soil types (IUSS Working Group WRB, 2007) formed on the Pleistocene glacial bedload are Cambisols and Stagnosols. The climate of the Pleistocene (period) also created vast extents (approx. 15 %) of Histosols. The mean annual temperature is 8.9 °C, and the mean annual precipitation is 660 mm (German Meteorological Service (DWD), data obtained from the Climate Data Center, reference period 1988–2018) (Koch et al., 2019). The hydrology of the catchment is markedly influenced by artificial drainage. Approximately 88 % of the Zarnow catchment is drained by subsurface or ditch drainage. Further detailed information on the study site and the long-term monitoring activities in place there is provided in Nausch et al. (2017), Tiemeyer

et al. (2009, 2006), and Zimmer et al. (2016). For the present study, we used samples taken from the beginning of November 2019 to the end of April 2020 to cover the principal discharge period. No fertilizer application took place within the study period. Water samples at different locations draining different areas—i.e., drain outlet (4.2 ha catchment area), ditch (179 ha catchment area), and brook (1550 ha catchment area)—were taken automatically (Teledyne Isco, Inc., Lincoln, NE, USA) every 6 h and mixed to create a daily sample. Samples were collected every week. The sampling scheme is part of a hierarchical long-term monitoring site initiated in November 2003 (Tiemeyer et al., 2006) to observe spatial effects on nutrient exports from agricultural fields. Sampling was performed weekly, every Thursday. The collected water samples were stored in a cooling box, transported to the laboratory, and processed immediately to prevent alterations of the various P fractions. For this study, water samples were selected from the peak of all runoff events ($n = 13$) within the runoff period and for four representative baseflows. All samples were kept unfiltered or were filtered using pre-combusted (6 h, 450 °C) 0.75 μm cellulose acetate membrane filters (Carl Roth GmbH, Karlsruhe, Germany). The filtered samples for AF^4 analyses (see below) were stored in polyethylene terephthalate tubes, shock-frozen immediately after filtration using liquid nitrogen in a cryogenic storage dewar, and subsequently stored at −20 °C.

The soil samples were collected from an adjacent arable field located in the catchment area of the sampled tile-drainage system. The samples were taken from three soil horizons (Ap, Bw, and C) with nine replicates. The sampling locations were located upslope (150 m away from the drainage ditch), midslope (100 m away from the drainage ditch), and downslope (30 m away from the drainage ditch). The nine replicates were at least 3 m apart. All sampling locations were within the drainage field of the drainage sampling station under observation. The disturbed soil samples were collected with an auger (Edelmann-Bohrer, Eijkelkamp Agrisearch Equipment, Giesbeek, Netherlands) and stored in plastic bags. The collected soil samples were air-dried and passed through a 2 mm sieve before soil colloid extraction.

The water level and discharge at the collector drain outlet were measured with a Venturi flume (Eijkelkamp Agrisearch Equipment, Giesbeek, Netherlands). The sampling station of the drainage ditch was equipped with an ultrasonic water level measurement device (Teledyne Isco, Inc., Lincoln, NE, USA). At the Zarnow measurement station, the water level was measured with a pressure sensor (UGT GmbH, Müncheberg, Germany). The water level was measured every 15 min and averaged to obtain a daily mean value. The discharge was measured weekly using an inductive flowmeter (Flo-Mate™, Marsh-McBirney, Inc., Frederick, MD, USA) to set up semi-annual rating curves for the ditch and brook stations.

A simple baseflow separation routine was used to subdivide streamflow data into fast (event flow) and slow (baseflow) components. Baseflow was separated from the total daily discharge (Fig. 1) using a recursive digital filter (Lyne and Hollick, 1979; Nathan and McMahon, 1990). The filter is of the form:

$$f_k = \propto f_{k-1} + \frac{(1+\propto)}{2}(y_k - y_{k-1}) \quad (1)$$

where f_k is the filtered quick response at the k^{th} sampling point, y_k is the original discharge, and α is the filter parameter set to 0.925 as recommended by Nathan and McMahon (1990).

Flow events were defined as periods where the peak flow exceeded the baseflow by a factor of at least 1.5, resulting in a total of 13 different flow events (Fig. 1). After modeling the baseflow curve, we selected four points distributed over the entire discharge period where the drain discharge was at or near the modeled baseflow; these served as a control sample for comparison with the event flow (Fig. 1).

2.2. General analyses and soil colloid extraction

All size fractions obtained and analyzed in this study are summarized and explained in the supplementary information (Table S1). In short, seven different size fractions were analyzed for the water samples, and three different size fractions for the soil samples. For the water samples, we analyzed the truly dissolved total P (truly DP), colloidal P <750 nm ($TP_{colloids}$), total particulate P >750 nm ($TP_{>750\ nm}$, calculated based on total P (TP) in unfiltered samples minus $TP_{colloids}$), and TP in unfiltered samples, including dissolved and particulate P ($TP_{unfiltered}$). Using AF^4, water colloids <750 nm were further size fractionated into three different size fractions, namely water colloids between 0.66 and 20 nm (water $colloids_{0.66–20nm}$), water colloids between 20 and 60 nm (water $colloids_{20–60nm}$), and water colloids between 60 and 750 nm (water $colloids_{60–750nm}$). For the soil samples, we analyzed water-dispersible colloids (WDCs) only and fractionated them using AF^4 into three different size fractions, namely soil colloids between 0.66 and 20 nm (soil $colloids_{0.66–20nm}$), soil colloids between 20 and 100 nm (soil $colloids_{20–100nm}$), and soil colloids between 100 and 450 nm (water $colloids_{100–450nm}$). For all AF^4 size fractions, not only P but also other elements were analyzed (see next section on AF^4 analysis).

The $TP_{unfiltered}$ concentration in water samples was determined by means of alkaline persulphate oxidation (Koroleff, 1983). Briefly, the unfiltered sample was mixed with a solution of $K_2S_2O_8$, H_3BO_3, and NaOH digested in a microwave (Mars 5, CEM GmbH, Germany). After adding ascorbic acid ($C_6H_8O_6$) and ammonium heptamolybdate, the sample was measured colorimetrically at a wavelength of 885 nm (CFA, AA3 with xy2 autosampler, Seal Analytical GmbH, Germany).

The P loss rates L (kg ha^{-1} d^{-1}) were calculated as described in Tiemeyer et al. (2006), by using the P concentration c (mg L^{-1}) and flow rate Q (mm d^{-1}) for the equation

$$L = \frac{cQ}{100} \quad (2)$$

By establishing a linear regression (Fig. S1) between the measured loss rates and daily discharge, the loss rates could be calculated for days for which only the discharge was available.

WDC extraction from soils was performed by combining wet sieving with centrifugation. In brief, 10 *g* air-dried soil (<2 mm) was immersed in deionized water on the top of a sieve stack (with sieve mesh sizes 20, 53, and 250 μm). The soil particles were separated by manually shaking the sieves up and down. The 250 μm mesh-size sieve and the soil fractions retained were removed when the water passing through the sieve ran clean. The same procedure was repeated for the 53 and 20 μm sieves. The soil suspension containing the <20 μm size fraction was collected and used for WDC extraction using centrifugation. The centrifugation parameters (4000 rcf for 5 min) were calculated with reference to Stokes' law (Henderson et al., 2012) to obtain colloids <450 nm. The volume of the resulting soil suspensions was recorded for the purpose of calculating the colloidal elemental concentration.

2.3. Asymmetric flow field-flow fractionation of water and soil samples

Both the colloids in the collected water and soil samples and the WDCs were size separated using AF^4 (Postnova Analytics, Landsberg, Germany). The C_{org} content in the different colloidal size fractions was measured using AF^4 coupled both to a UV–vis detector with an absorption wavelength of 254 nm (Postnova Analytics) and to an organic carbon detector (OCD; DOC-Labor GmbH, Germany). The element concentrations of P, Fe, Al, Si, Ca, and Mg in each size fraction were determined by AF^4 coupled to an inductively coupled plasma mass spectrometer (ICP-MS; Agilent 7500, Agilent Technologies, Japan) using post-channel calibration with Rh as the internal standard (Nischwitz et al., 2016). Details of the AF^4 separation method are presented in Table S2, while details of the coupling to the ICP-MS and OCD detectors can be found in Gottselig et al. (2017a) for the water samples and in Krause et al. (2020) for the soil samples.

The lowest size limit of 0.66 nm was established by the cutoff of the used membrane (1 kDa). Reference materials (Suwanee River NOM, Humic Acid Standard II, and Fulvic Acid Standard II, International Humic

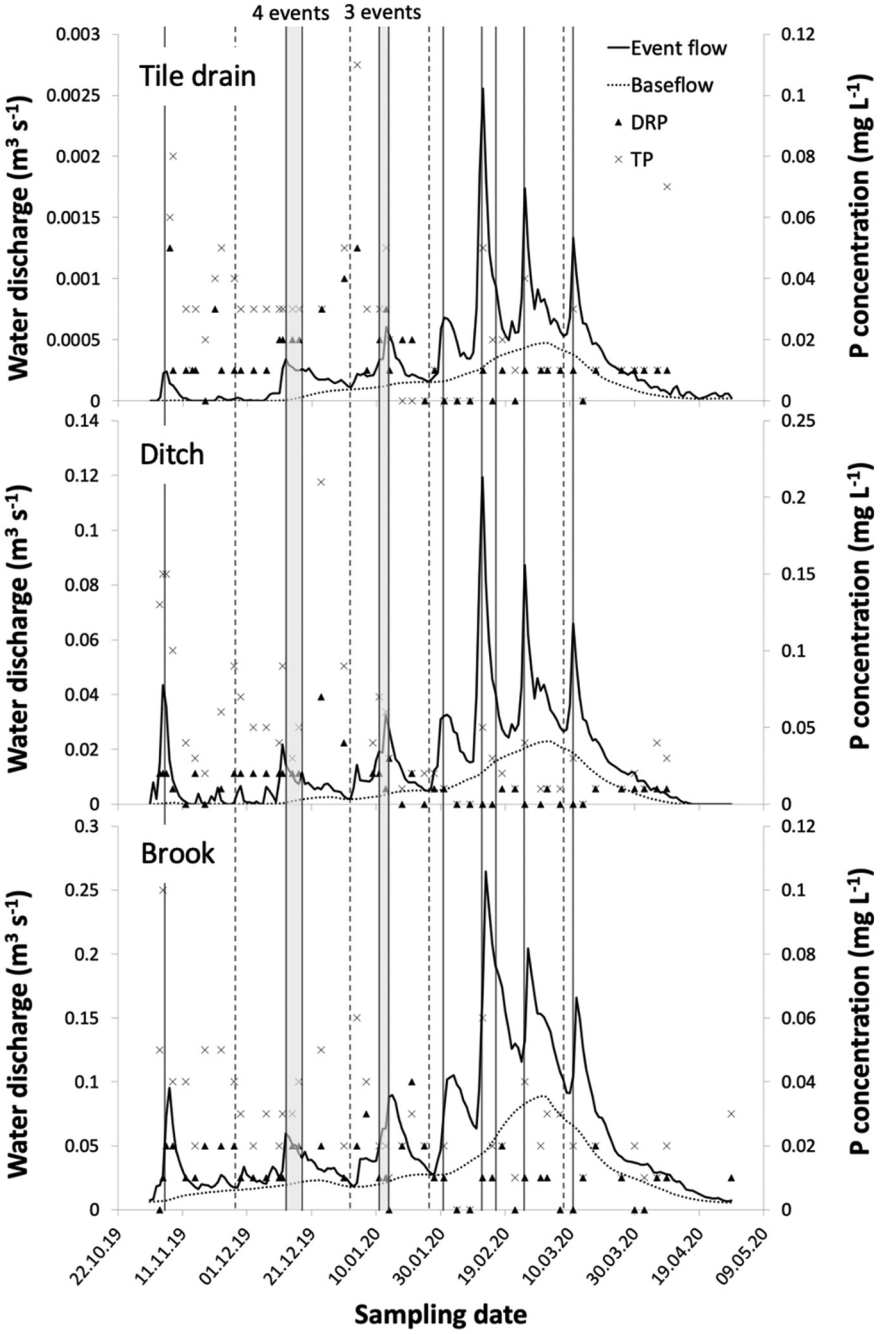

Fig. 1. Measured flow, fitted baseflow, dissolved reactive P (DRP), and total P (TP) during the study period (2019/2020) at three sampling stations: tile drain, ditch, and brook. Vertical broken lines mark the sampling points of the baseflow, while vertical bold lines mark the sampling points of the specific flow events (1 to 13) for subsequent measurements. The gray highlighted areas show several sampled events.

Substances Society, Denver, USA; Sulfate Latex Standards 8 % *w/v* 21–630 nm; Postnova Analytics, Landsberg, Germany) were used with the same AF^4 conditions used for the samples for calibration of the particle diameters included in each size fraction. The Humic Acid Standard II and the Fulvic Acid Standard II were also used for C_{org} quality control by comparing results with previous measurements of these standards. However, no reference material exists that covers the diverse particle morphologies and elemental concentrations of environmental samples. Therefore, the specified hydrodynamic diameters of the particles are equivalent sizes based on the elution time of the reference materials. For the water samples, the first fraction was estimated based on calibration with the reference materials to include nanoparticles between 0.66 nm (membrane molecular weight cutoff) and 20 nm, and the second fraction to include nanoparticles >20 to 60 nm. Furthermore, dynamic light scattering revealed that the third fraction included nanoparticles >60 nm to fine colloids up to the upper size cutoff of the filter (750 nm). For soil colloids, the size fractions were also calibrated according to latex standards; the first size fraction ranged from 0.66 to 20 nm, the second size fraction from 20 to 100 nm, and the third size fraction from 100 to 450 nm, which was the size cutoff set for centrifugation. Because the AF^4 technique does not recover dissolved species, total element recovery of aqueous water phases was not assessed in the same run. However, by measuring without AF^4 fractionation (zero crossflow), it is possible to determine total elemental concentrations using the AF^4 system. In the filtered and unfractionated samples, the total elemental concentrations of P, Fe, Al, Si, Ca, and Mg were determined using ICP-MS (Agilent 7500, Agilent Technologies), as described above.

2.4. Statistical analyses

Statistical analyses were performed in Excel (Excel 2016, Microsoft Corporation, Washington, USA) using XLSTAT 2021.5 (Addinsoft, Paris, France), as well as in Origin(Pro) 2022 (OriginLab Corporation, Northampton, MA, USA) and RStudio 3.6.3. For the water samples, we tested proportions of particulate elemental concentrations of colloids <750 nm in relation to total elemental concentrations of colloids <750 nm, testing for normal distribution using the Shapiro–Wilk test ($p < 0.05$) and for homogeneity of variances using the Brown–Forsythe test ($\alpha = 0.05$). The differences between sampling locations were determined by means of a one-way ANOVA ($\alpha = 0.05$). If significant differences occurred, we used the Tukey HSD test to perform a post-hoc separation of means ($\alpha = 0.05$). The similarity or dissimilarity between the time-series data of the three sampling sites was evaluated based on the Euclidean distance. The P stocks from colloids extracted from the soil samples were tested using a multilevel model, as both variables used (horizons and size fractions) violated the data independence assumption. The modeling work was performed using the *lme()* function from the R package "*nlme*". Both variables (horizons and fractions) and their interactions (horizons × fractions) were added into the baseline model successively. The maximum likelihood method (ML) was used to identify the best model. Post-hoc tests were performed for significant effects ($p < 0.05$). To identify (i) the fraction-specific preferential binding of P and (ii) the origin of water colloids in the adjacent field, a hierarchical tree cluster analysis as described in Gottselig et al. (2017b)—with 1 − Pearson's r as the distance measure, with the complete linkage rule, and without normalization—was applied to the element concentrations obtained for the AF^4-separated particle size fractions of water and soil colloids. In contrast to statistical significance testing, cluster analyses use algorithms that group parameters with the greatest similarity based on the available samples at the start of the analysis. Subsequently, the threshold for deciding when to declare two or more objects to be members of the same cluster is lowered.

3. Results

3.1. Discharge and total P losses

The total precipitation of 197 mm in the discharge period 2019/2020 was equal to that recorded in the discharge period 2013/2014 (Nausch et al., 2017). However, it amounted to only 74 % and 69 % of that recorded in the discharge periods 2003/2004 and 2005/2006, respectively (Tiemeyer et al., 2009), or only 29 % of the long-term annual average of 689 mm. Rainfall of ≥6.0 mm day^{-1} took place in the first week of November and between 31.01.2020 and 13.03.2020 (Fig. S2). These rainfall events generated discharge peaks in the tile drain, ditch, and brook, while the later rain events in particular led to an increase in discharge (Fig. 1). For the tile drain, ditch, and brook, the proportion of modeled baseflow to total flow amounted to 15, 17, and 42 %, respectively, which confirms expectations that the brook is groundwater driven. The mean TP concentrations in the unfiltered samples ($TP_{unfiltered}$) were comparable for each sampling station (tile drain: 0.046 mg L^{-1}, ditch: 0.027 mg L^{-1}, brook: 0.030 mg L^{-1}). Over the complete sampling period 2019/2020, the lowest area-normalized $TP_{unfiltered}$ losses (g ha^{-1}) were found for the brook and the highest were found for the ditch (Table 1).

3.2. Truly DP, $TP_{colloids}$, and $TP_{>750\ nm}$ in water samples

To characterize the total P composition of the unfiltered water samples in more detail, the samples were split into three fractions: truly DP, particulate P <750 nm ($TP_{colloids}$), and particulate P >750 nm ($TP_{>750\ nm}$). The TP concentrations, as well as their proportions of $TP_{unfiltered}$, were determined separately (Table 2). Taking all events into account, it was found that at all three sampling stations, the mean shares of the three P fractions in the overall P loss were similar. The majority of $TP_{unfiltered}$ was formed by $TP_{>750\ nm}$ (54 % ± 28; 55 % ± 21; 59 % ± 24), followed by truly DP (37 % ± 21; 38 % ± 19; 34 % ± 32), and by a rather small contribution of $TP_{colloids}$ (5 % ± 2; 6 % ± 4; 6 % ± 2) (tile drain, ditch, and brook, respectively; Table 2). Thus, during flow events, 63–66 % of $TP_{unfiltered}$ was present as particulate P ($TP_{>750\ nm}$ + $TP_{colloids}$), whereas during baseflow this figure amounted to 97–99 %. This was reflected in an even more pronounced dominance of $TP_{>750\ nm}$ during baseflow conditions (82–92 % of $TP_{unfiltered}$), while truly DP during baseflow was almost negligible (1–3 % of $TP_{unfiltered}$). The mean proportions of $TP_{colloids}$ in the ditch and brook during baseflow (7 % ± 6; 7 % ± 4) were comparable to those recorded during flow events. In contrast, for the tile drain, the mean proportions of $TP_{colloids}$ at baseflow (15 % ± 17 of $TP_{unfiltered}$) were higher when compared to both the flow events and to the other sampling stations. However, this was not significant, since this higher proportion was mostly due to the high initial peak in the proportion of $TP_{colloids}$ (41 % of $TP_{unfiltered}$) during the early stages of baseflow formation at the onset of the discharge period, while $TP_{>\ 750\ nm}$ peaked during the very first flow event. After the occurrence of these peak concentrations and proportions of $TP_{colloids}$ (baseflow) and $TP_{>750\ nm}$ (flow events), the values dropped and remained at a similar level (Table 2).

Considering the change in the proportions of $TP_{>750\ nm}$, $TP_{colloids}$, and truly DP during the runoff period, it is obvious that the proportions remained relatively constant during baseflow, but were subject to strong fluctuations during event flow. For the latter, the observed variations in the composition of $TP_{unfiltered}$ were mainly caused by $TP_{>750\ nm}$ and truly DP, while the proportions of $TP_{colloids}$ remained at a relatively constant level.

3.3. Elemental loads in water samples

Taking into account all sampling stations, flow regimes, and colloidal size fractions obtained by AF^4 measurements, the colloidal elemental loads in the <750 nm filtrate (water $colloids_{0.66–750\ nm}$) followed the order Al ≤ P < Fe ≤ Si < Mg < C_{org} < Ca (Tables S3, S4). The proportion of the respective colloidal elemental load in relation to the total elemental load in the <750 filtrate (colloidal + truly dissolved load) was similar between flow events (13 to 27 %). However, during baseflow, the mean proportion of colloidal P and Al differed significantly at 85 and 100 %,-respectively, while the other elements were in the range of 9 to 30 % (Table 3). There were also no significant changes in the proportions of colloidal loads between the three sampling stations, with the exception of

Table 1
Water discharge, drainage area, P loss rates of total P ($TP_{unfiltered}$), particulate P >750 nm ($TP_{>750\ nm}$), colloidal P ($TP_{colloids}$), and truly dissolved P (truly DP), as well as the coefficient of determination (R^2) of P loss rates (g ha^{-1} d^{-1}) from discharge (mm d^{-1}).

	$TP_{unfiltered}$			$TP_{>750\ nm}$			$TP_{colloids}$			Truly DP		
	Tile drain	Ditch	Brook	Tile drain	Ditch	Brook	Tile drain	Ditch	Brook	Tile drain	Ditch	Brook
Discharge (mm over the period 2019/2020)	120	137	60	120	137	60	120	137	60	120	137	60
Drainage area (ha)	4.2	179	1550	4.2	179	1550	4.2	179	1550	4.2	179	1550
Area-normalized loss rate (g ha^{-1} over the period 2019/2020)	48	55	18	36	41	12	2	3	1	11	1	5
Loss rate (g over the period 2019/2020)	**202**	**9774**	**27677**	**151**	**7330**	**18451**	**10**	**489**	**1845**	**45**	**244**	**7380**
R^2	0.835	0.806	0.575	0.851	0.823	0.655	0.939	0.978	0.747	0.830	0.926	0.585
p Value	<0.001	<0.001	0.003	<0.001	<0.001	0.003	<0.001	<0.001	<0.001	<0.001	<0.001	0.003

Table 2
Concentrations of total P ($TP_{unfiltered}$), total P in particles >750 nm ($TP_{>750\ nm}$, calculated by subtracting $TP_{colloids}$ and truly DP from $TP_{unfiltered}$), total P in colloids <750 nm ($TP_{colloids}$), and truly dissolved P (truly DP), as well as the proportions of $TP_{>750\ nm}$, $TP_{colloids}$, and truly DP to $TP_{unfiltered}$ (%) for baseflow and flow events for the three sampling stations: tile drain, ditch, and brook. n.d. = not detected.

Time of sampling	Tile drain				Ditch				Brook			
	$TP_{unfiltered}$	$TP_{>750\ nm}$	$TP_{colloids}$	Truly DP	$TP_{unfiltered}$	$TP_{>750\ nm}$	$TP_{colloids}$	Truly DP	$TP_{unfiltered}$	$TP_{>750\ nm}$	$TP_{colloids}$	Truly DP
	mg L^{-1}(%)	μg L^{-1}(%)	μg L^{-1}(%)	μg L^{-1}(%)	mg L^{-1}(%)	μg L^{-1}(%)	μg L^{-1}(%)	μg L^{-1}(%)	mg L^{-1}(%)	μg L^{-1}(%)	μg L^{-1}(%)	μg L^{-1}(%)
Baseflow 1	0.03	15.55 (52)	12.15 (41)	2.29 (8)	0.07	67.06 (96)	2.67 (4)	0.27 (0)	0.03	25.46 (85)	3.89 (13)	0.65 (2)
Baseflow 2	0.05	48.91 (98)	0.95 (2)	0.13 (0)	0.09	88.55 (98)	1.34 (1)	0.11 (0)	0.02	18.84 (94)	0.88 (4)	0.28 (1)
Baseflow 3	0.01	8.92 (89)	0.84 (8)	0.24 (2)	0.02	18.53 (93)	1.34 (7)	0.13 (1)	0.01	9.19 (92)	0.71 (7)	0.10 (1)
Baseflow 4	0.01	9.11 (91)	0.78 (8)	0.11 (1)	0.01	8.47 (85)	1.44 (14)	0.09 (1)	0.02	19.16 (96)	0.76 (4)	0.09 (0)
Mean baseflow (%)		82 ± 21	15 ± 17	3 ± 3		93 ± 6	7 ± 6	1 ± 0		92 ± 5	7 ± 4	1 ± 1
Event 1	0.08	69.29 (87)	1.99 (2)	8.72 (11)	0.10	80.59 (81)	2.42 (2)	16.99 (17)	0.04	36.34 (91)	1.47 (4)	2.19 (5)
Event 2	0.03	17.25 (58)	1.47 (5)	11.27 (38)	0.04	22.14 (55)	1.94 (5)	15.91 (40)	0.02	9.44 (47)	1.18 (6)	9.39 (47)
Event 3	0.03	19.77 (66)	1.79 (6)	8.45 (28)	0.09	74.13 (82)	1.79 (2)	14.07 (16)	0.03	17.54 (58)	1.62 (5)	10.85 (36)
Event 4	0.03	4.82 (16)	3.01 (10)	22.17 (74)	0.03	4.66 (16)	2.66 (9)	22.68 (76)	0.03	10.80 (36)	2.39 (8)	16.81 (56)
Event 5	0.03	16.72 (56)	1.23 (4)	12.06 (40)	0.05	29.99 (60)	1.98 (4)	18.03 (36)	0.04	30.03 (75)	1.43 (4)	8.54 (21)
Event 6	0.03	18.12 (60)	1.60 (5)	10.28 (34)	0.07	51.78 (74)	2.43 (3)	15.79 (23)	0.02	8.34 (42)	1.64 (8)	10.02 (50)
Event 7	0.05	37.41 (75)	1.70 (3)	10.89 (22)	0.06	40.12 (67)	2.18 (4)	17.70 (29)	0.02	12.45 (62)	1.57 (8)	5.98 (30)
Event 8	0.02	2.83 (14)	1.71 (9)	15.46 (77)	0.03	6.00 (20)	2.15 (7)	21.85 (73)	0.01		1.81 (18)	16.72 (167)
Event 9	n.d.		1.44	1.26	0.01	4.39 (44)	1.90 (19)	3.71 (37)	0.02	17.20 (86)	1.54 (8)	1.26 (6)
Event 10	0.05	37.42 (75)	2.08 (4)	10.50 (21)	0.05	32.97 (66)	2.45 (5)	14.57 (29)	0.06	49.20 (82)	2.32 (4)	8.48 (14)
Event 11	0.02	8.29 (41)	1.44 (7)	10.27 (51)	0.03	13.04 (43)	2.29 (8)	14.66 (49)	0.02	11.28 (56)	1.41 (7)	7.31 (37)
Event 12	0.04	30.76 (77)	1.65 (4)	7.59 (19)	0.04	24.58 (61)	2.30 (6)	13.12 (33)	0.04	30.98 (77)	2.06 (5)	6.96 (17)
Event 13	0.03	23.14 (77)	1.68 (6)	5.18 (17)	0.03	15.22 (51)	2.24 (7)	12.55 (42)	0.02	11.40 (57)	1.61 (8)	6.98 (35)
Mean event (%)		54 ± 28	5 ± 2	37 ± 21		55 ± 21	6 ± 4	38 ± 19		59 ± 25	6 ± 2	34 ± 23

C_{org}, which showed significantly higher proportions within the ditch compared to the tile drain and the brook during flow events (Table 3).

3.4. Distribution pattern of P within water colloids$_{0.66–750nm}$

The colloidal size fraction studied here (water colloids$_{0.66–750nm}$) was mainly present in three size fractions (Table S3). During flow events, the main proportions of $TP_{colloids}$ (67 to 73 %) were found in the water colloids$_{60–750nm}$, followed by water colloids$_{20–60nm}$ (26 to 32 %), with minor contributions (<1 %) in water colloids$_{0.66–20nm}$. However, during baseflow, the mean proportions of water colloids$_{20–60nm}$ increased to 42–47 %, whereas the proportions of water colloids$_{60–750nm}$ decreased to 51–58 % (data not shown). In terms of the sampling stations, significantly higher mean proportions of $TP_{colloids}$ were found in water colloids$_{20–60nm}$ (lower in water colloids$_{60–750nm}$) from the ditch compared to the tile drain and brook during flow events, while at baseflow this difference was only significant between the ditch and tile drain. Based on the calculation of the Euclidean distance, the time course of the proportions of all size fractions was more similar between the tile drain and brook, regardless of the flow regime. However, the absolute difference between sampling stations was generally larger for events than for baseflow conditions. There was no visible trend in the time course of the distribution pattern of P within the three size fractions during flow events, while a trend of decreasing proportions of water colloids$_{0.66–20nm}$ and water colloids$_{20–60nm}$ with time, as well as increasing proportions of water colloids$_{60–750nm}$ with time, was indicated during baseflow.

Table 3
Proportions of colloidal loads (<750 nm, samples analyzed using AF^4) in relation to total elemental loads (dissolved + colloidal <750 nm, samples analyzed using AF^4) for the different flow regimes for the three sampling stations: tile drain, ditch, and brook, as well as the mean of all sampling stations (all stations). Significant differences ($p < 0.05$) between stations and within flow regimes are marked with superscript letters.

	C_{org}	P	Fe	Al	Si	Ca	Mg
	% colloidal						
Baseflow							
Tile drain	10^a	84^a	11^a	64^a	28^a	9^a	7^a
Ditch	13^a	92^a	17^a	100^b	25^a	11^a	9^a
Brook	6^a	85^a	18^a	71^a	37^a	14^a	11^a
All stations	10	87	15	79	30	11	9
Flow events							
Tile drain	12^a	17^b	22^b	15^c	31^a	15^a	14^a
Ditch	21^b	14^b	20^a	14^c	26^a	13^a	12^a
Brook	9^a	21^b	23^b	21^c	23^a	15^a	13^a
All stations	14	17	22	17	27	14	13

3.5. Associations of P with other elements

Hierarchical tree cluster analysis generally revealed three clusters for all size fractions (Table 4). When all stations under event flow conditions were included in the cluster analysis, P clustered mainly with Al, Fe, Mg, and Si in water colloids$_{0.66–20nm}$, with Al and Si in water colloids$_{20–60nm}$, and with Al, Fe, and Si in water colloids$_{60–750nm}$. When the results of the cluster analysis

Table 4
Hierarchical tree cluster analysis with 1 – Pearson's r as the distance measure and complete linkage. For water colloids, analysis was performed for all sampling stations, size fractions (1st: 0.66 to 20 nm; 2nd: 20 to 60 nm; 3rd: 60 to 750 nm), and flow events. For stocks of soil colloids, analysis was performed for all soil horizons and size fractions (1st: 0.66 to 20 nm; 2nd: 20 to 100 nm; 3rd: 100 to 450 nm) . Numbers in parentheses indicate the 1 – Pearson's r distance. A low linkage distance value indicates stronger potential binding.

Sampling station & horizon	Number of cluster and elements			Number of cluster and elements			Number of cluster and elements		
	1	2	3	1	2	3	1	2	3
	First size fraction			Second size fraction			Third size fraction		
Tile drain	C_{org}/Mg (0.42)	**P**/Al/Fe/Si (0.574)	Ca (1.94)	**P**/Al/Si (0.17)	Fe/Ca/Mg (0.25)	C_{org} (0.57)	Mg/Ca (0.13)	Fe/Al/Si (0.28)	**P**/C_{org} (0.64)
Ditch	Si/Ca (0.00)	**P**/Al/Fe/Mg (0.24)	C_{org} (0.93)	**P**/Al/Fe/Mg (0.17)	Al/Si (0.22)	C_{org} (1.37)	Mg/Ca (0.15)	Fe/Al/Si (0.50)	**P**/C_{org} (1.08)
Brook	**P**/Al/Fe/Mg (0.28)	C_{org}/Ca (0.62)	Si (1.10)	**P**/Al/Mg (0.32)	Fe/Ca/Si (0.72)	C_{org} (1.38)	P/Si (0.44)	Fe/Ca/Al/Mg (0.67)	C_{org} (1.36)
All stations	**P**/Al/Fe/Mg/Si (0.38)	C_{org}/Ca (0.48)		Fe/Ca/Mg (0.34)	P/Al/Si (0.58)	C_{org} (1.01)	Mg/Ca (0.22)	**P**/Al/Fe/Si (0.65)	C_{org} (1.23)
Ap	Al/Fe/Si (0.008)	**P**/Mg/Ca/C_{org} (0.791)		**P**/Mg/Ca/Al/Fe/Si (0.454)	C_{org} (1.106)		**P**/Mg/Ca/Al/Fe/Si (0.762)	C_{org} (1.640)	
Bw	Al/Fe/Si (0.021)	**P**/Mg/Ca/C_{org} (0.784)		**P**/Mg/Ca/Al/Fe/Si (0.299)	C_{org} (1.822)		Mg/Ca/Al/Fe/Si/C_{org} (0.453)	**P** (1.165)	
C	**P**/C_{org} (0.693)	Mg/Ca/Al/Fe/Si (0.693)		**P**/Mg/Ca/Al/Fe/Si (0.139)	C_{org} (0.604)		Mg/Ca/Al/Fe/Si/C_{org} (0.509)	**P** (1.239)	
All horizons	Mg/Ca/Al/Fe/Si (0.306)	**P**/C_{org} (0.441)		**P**/Mg/Ca/Al/Fe/Si (0.072)	C_{org} (0.336)		Mg/Ca/Al/Fe/Si/C_{org} (0.068)	**P** (0.368)	

were considered separately for the individual stations and flow regimes, the tile drain showed a noticeably different cluster composition, with P sharing a cluster with Al, Fe, and Si; for the ditch and brook, however, P clustered with Al, Fe, and Mg. For water colloids$_{20–60nm}$, all P clusters exhibited a different composition between sampling stations, with Si once again only being present in the tile drain cluster. In water colloids$_{60–750nm}$, P clustered exclusively with C_{org} in the tile drain and in the ditch, while it clustered with Si in the brook (Table 4).

Hierarchical tree cluster analysis revealed no connection between water colloids$_{0.66–20nm}$, water colloids$_{20–60nm}$, and water colloids$_{60–750nm}$, as each size fraction formed a separate cluster (Fig. 2). Within the three size fraction clusters, there is a clear separation between the ditch, tile drain, and brook, with the ditch forming a separate cluster while the tile drain and brook are grouped within a single cluster, irrespective of events. This is different for water colloids$_{20–60nm}$, where the brook and tile drain form a cluster under baseflow conditions, while the ditch (during both baseflow and flow events) clusters with the tile drain and brook under flow event conditions. For water colloids$_{60–750nm}$, all three sampling stations form a cluster under flow event conditions; under baseflow conditions, meanwhile, the ditch and the brook cluster, and the tile drain forms a separate cluster (Fig. 2).

3.6. Composition of soil colloids and fate in water

Generally, as for the water colloids, three size fractions were identified for the soil colloids, namely soil colloids$_{0.66–20nm}$, soil colloids$_{20–100nm}$, and soil colloids$_{100–450nm}$ (Tables S1, S5). The colloidal P stocks for the three size fractions were 1.3 to 4.4 kg ha^{-1}, 0.6 to 1.7 kg ha^{-1}, and 3.6 to 5.1 kg ha^{-1} for the Ap, Bw, and C horizons, respectively (Fig. 3 and Table S5). The highest P concentrations were found in soil colloids$_{0.66–20nm}$ from the Ap horizon, while the C horizon exhibited the highest P stocks in soil colloids$_{20–100nm}$ and soil colloids$_{100–450nm}$. Between the size fractions, colloidal P stocks in soil colloids$_{20–100nm}$ were significantly lower than those in soil colloids$_{0.66-20nm}$ and soil colloids$_{100–450nm}$ for both the Ap and Bw horizons, while these were not significant for the C horizon (Fig. 3).

Hierarchical tree cluster analysis of soil colloids generally revealed two clusters for all three size fractions (Table 4). When all three horizons (Ap, Bw, C) were grouped in a cluster analysis (All), P mainly clustered with C_{org} in soil colloids$_{0.66–20nm}$ and with all elements except C_{org} in soil colloids$_{20–100nm}$, and formed a separate cluster in soil colloids$_{100–450nm}$. Results of the cluster analysis conducted on soil horizon samples revealed that in soil colloids$_{0.66–20nm}$, P mainly clustered with C_{org}, while in the Ap and Bw horizons, Mg and Ca were also part of the P cluster. For soil colloids$_{20–100nm}$, the results were identical for all soil horizons with P and Mg/Ca/Al/Fe/Si clustering together, while C_{org} formed a separate cluster. In soil colloids$_{100–450nm}$, the results differed between Ap and the other horizons, with P clustering with all elements except C_{org} in the Ap horizon and forming a separate cluster in the Bw and C horizons (Table 4).

In order to estimate the origin of water colloids within the adjacent soil, we conducted a hierarchical tree cluster analysis of both water and soil colloid concentrations (both in μg L^{-1}). This analysis revealed three main clusters, with soil colloids$_{20–100nm}$ and soil colloids$_{100–450nm}$ from all soil horizons—i.e., Ap, Bw, C—clustering together in cluster 1. Cluster 2 included water colloids$_{20–60nm}$ for all sampling stations, i.e., tile drain, ditch, and brook, as well as soil colloids$_{0.66–20nm}$ from the C horizon. In cluster 3, soil colloids$_{0.66–20nm}$ from the Ap and Bw horizons clustered with water colloids$_{0.66–20nm}$ and water colloids$_{60–750nm}$. The distance measure of soil colloids from the C horizon to the water colloids was smaller than for the Ap and Bw horizons, indicating that there were more similarities between soil colloids$_{0.66–20nm}$ from the C horizon and water colloids$_{20–60nm}$ (Fig. S3).

4. Discussion

4.1. Precipitation, discharge, and P transport at the monitoring stations

The initial peak of particulate P loss at all sampling stations during the first rain event at the beginning of the discharge period (Table 2) was also observed for other hydrological discharge periods at the same site (Nausch et al., 2017) and was reported by others from irrigation experiments (de Jonge et al., 2004; Kjaergaard et al., 2004; Schelde et al., 2002; Zhuang et al., 2007). This can be explained by a re-mobilization of particulate P, especially of particles >750 nm, which settled in the drain and ditch during dry fall outside of the discharge season and were subsequently transported further downstream. After the first event in the subsequently sampled baseflow, the load of $TP_{>750\ nm}$ in the tile drain was lower, whereas for $TP_{colloids}$ <750 nm it remained at the same level. This suggests that the re-mobilization potential was exhausted faster for particles >750 nm than for colloids <750 nm that were continuously mobilized at the same rate. Event flow particularly affected the transport of $TP_{>750\ nm}$, leading mainly to an effect of varying discharge intensity and thus straining and attachment at the solid–water interface (Wang et al., 2020). This effect is greater for larger particles, as these particles are more prone to get stuck when the pore space is too small to admit them.

A colloidal export of around 5 to 6 % of $TP_{unfiltered}$ is in line with the findings of Burger et al. (2021) for exports from a forested headwater catchment after winter precipitation events with a mean precipitation of 3 mm

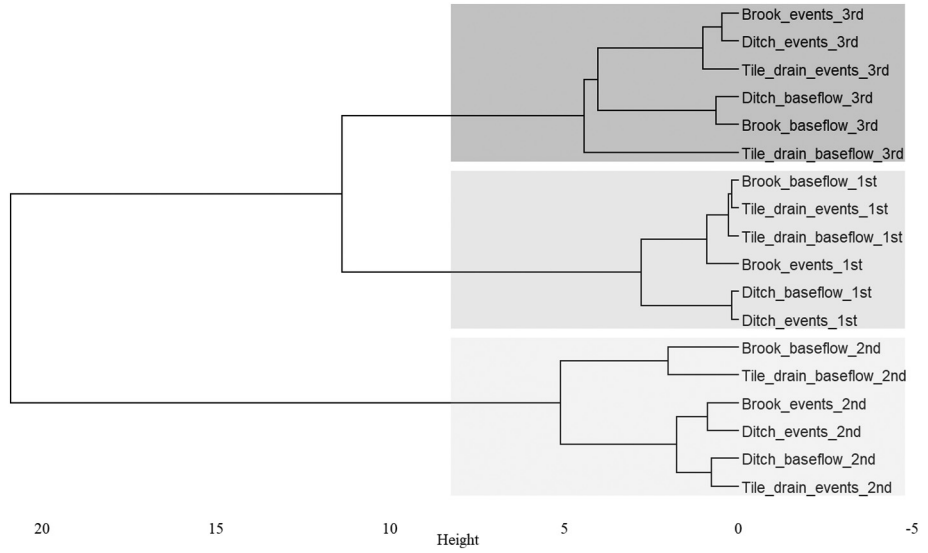

Fig. 2. Dendrogram of a hierarchical tree cluster analysis based on elemental colloidal composition in three size fractions (1st: 0.66 to 20 nm; 2nd: 20 to 60 nm; 3rd: 60 to 750 nm) in water samples determined by AF4 analysis of samples obtained from the three different sampling stations during baseflow and flow events.

d^{-1} for the event under study. A dominance of colloidal P losses over dissolved losses during flow events, as reported by Schelde et al. (2002), was not observed in this study for $TP_{colloids}$ < 750 nm. However, when the $TP_{>750\ nm}$ fraction was considered, which by size definition also contains colloids <1000 nm, particulate P loss dominated at ~2 times higher than the dissolved loss. Although it is widely accepted that P is mainly transported in particulate form during storm events and high discharge periods, studies estimating the losses from catchments via truly DP (<1 nm) are still rare. However, there is a growing awareness that even during storm flow, proportions of truly DP can be high and can make up the dominant P fraction, accounting for up to 61 % of total P losses (Gu, 2017). In our study, although on average the majority of P (~50 %) during storm events at all stations was still lost via particles >750 nm, losses via truly DP accounted for more than one third of total P losses (Fig. S4).

When total P loss rates per hectare of this study are compared to those from previous hydrological discharge periods (Tiemeyer et al., 2009), it becomes obvious that P losses not only result from differences in the intensity and amount of precipitation, but also from differences in temporal or spatial precipitation patterns. Despite the fact that the total precipitation was comparable to that recorded in other hydrological discharge periods, the strength of events differed, leading to differences in the P discharge at single stations and thus also to differing P exports.

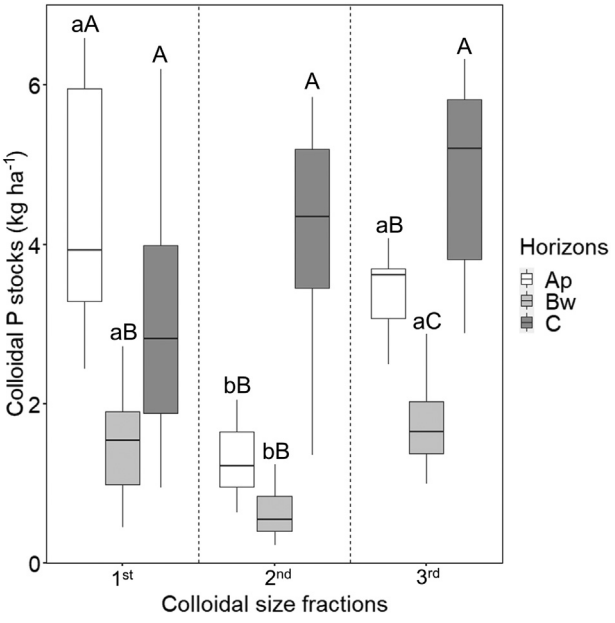

Fig. 3. Colloidal P stocks (kg ha^{-1}) of three size fractions (1st: 0.66 to 20 nm; 2nd: 20 to 100 nm; 3rd: 100 to 450 nm) in different soil horizons. Significant differences ($p < 0.05$) between size fractions but within the same soil horizon were labeled with lowercase letters, and between horizons but within the same size fraction with uppercase letters.

4.2. Composition of water colloids$_{0.66–750nm}$

The size ranges of the three dominant size fractions of water colloids identified in our study were in agreement with other studies analyzing natural colloids in watershed samples (Burger et al., 2021; Gottselig et al., 2014, 2017a, 2017b). The cluster analysis of elements regarding the size fractions separately but the sampling stations collectively (all stations combined) revealed that in water colloids$_{0.66–20nm}$, P mainly clustered with Al, Fe, Si, and Mg (Table 4), which hints at the presence of both of Fe/Al (hydr)oxides (Gottselig et al., 2017a; Hassellöv and von der Kammer, 2008; Jiang et al., 2015) and clay minerals with P adsorbed to them. In terms of the latter, the mineral composition of transported particles in the Zarnow catchment is, besides illite and illite-mixed layer minerals, known to be dominated by chlorites (Nausch et al., 2017), which are characterized by the presence of Fe/Mg silicates with a small amount of Al in the crystal structures (Hamer et al., 2003). The water colloids$_{20–60nm}$ were characterized by high concentrations of Fe, Al, Ca, and Mg, hinting at a mixed composition of clay minerals and Fe/Al (hydr) oxides. However, the clustering of P with Al and Si only indicates that P was adsorbed to the surfaces of clay minerals (most likely illite, given the missing Mg in the cluster) by means of ligand exchange with a metal hydroxide (Yaghi and Hartikainen, 2013), which is also corroborated by the soil pH of >7. The clustering of P with Al, Fe, and Si in water colloids$_{60–750nm}$ indicates associations with both Fe/Al (hydr)oxides and clay minerals like illite, which is due to the fact that the third peak, also called the release peak, can also contain smaller particles from water colloids$_{0.66–20nm}$ and water colloids$_{20–60nm}$ that were retained by the membrane during crossflow.

The influence of the sampling location factor (tile drain, ditch, or brook) on the composition of the clusters was strongest for water colloids$_{0.66–20nm}$ and water colloids$_{20–60nm}$. In the tile drain, P was mainly associated with

both clay minerals and hydroxides, while in the ditch and brook, the composition of the clusters hints at Fe/Al (hydr)oxides and Mg compounds that are not clay-associated, given the missing Si in the clusters. This fits with the results of suspended particulate matter (>800 nm) SEM-EDX analyses performed by Nausch et al. (2017) at the same sampling stations, which suggested that samples from the ditch and brook waters were enriched in Fe phosphates and that, for the brook in particular, clay minerals were underrepresented in the suspended matter, presumably due to sedimentation at times of low flow velocity. This indicates that, to some extent, the elemental composition of colloids at different sampling stations reflects the elemental composition of suspended particulate matter >800 nm, as colloids act as building units for larger size fractions (Totsche et al., 2018).

The composition of the P cluster of the ditch was consistently different for water colloids$_{0.66–20nm}$ and water colloids$_{20–60nm}$ compared to the tile drain and brook, irrespective of flow events. Cluster separation by sampling location and event (Fig. 2) revealed that especially in water colloids$_{0.66–20nm}$, the colloidal composition of the ditch was different to those of the tile drain and brook, presumably as a result of different forms and amounts of soil organic matter (SOM) due to an increased input of organic detritus into the ditch. The fact that nano-sized C_{org} clustered with Mg (tile drain) and Ca (brook) (Table 4) suggests that C═O groups of the SOM (e.g., carboxyl[ate] groups) can be assumed to be complexed and stabilized with divalent Ca^{2+} in the brook (Rowley et al., 2018) and divalent Mg^{2+} in the tile drain (Ellerbrock and Gerke, 2021). However, nano-sized C_{org} formed a separate cluster in the ditch, indicating that the majority of nano-sized C_{org} in the ditch may be fresh and not complexed. In general, the data obtained in our study confirms that the particulate but also the dissolved subsurface output of elements, particularly P, from the soil into the watershed is high, and is expected to dramatically increase during seasons with higher precipitation and a greater number of flow events.

4.3. Composition of water-extractable soil colloids

To identify the possible origin of colloids transported to the tile drain, ditch, and brook, we investigated water-extractable colloids from soils at various depths within the tile drain catchment. The higher stocks of colloidal P in the Ap horizon than in the Bw horizon (Fig. 3, Table S5) were caused by the enrichment of fertilizer P applied to the topsoil. Excess colloidal P could be transported from the topsoil to the subsoil via water-extractable colloids in intensively managed agricultural soils, especially in areas with surplus P fertilization (Chen and Arai, 2020; Rubæk et al., 2013).

When we examined the general composition of soil colloids as revealed by AF^4 analyses, the dominance of C_{org} in soil colloids$_{0.66–20nm}$ was in agreement with the results reported by others (Jiang et al., 2015; Krause et al., 2020). In this size fraction, P mainly clustered with either C_{org} or C_{org}/Ca/Mg, hinting at either organic P compounds or P-Ca/Mg-C_{org} complexes (Audette et al., 2016; Ellerbrock and Gerke, 2021; Gerke, 2010; Rowley et al., 2018). Cluster analysis of soil colloids$_{20–100nm}$ hints at an association of P with clay minerals and/or Fe/Al (hydr)oxides. A closer examination of the molar ratio between Si and Al revealed values between 1.7 and 2.3 (Table S6), indicating that 2:1 clay minerals such as illite were dominant. There was a slight (not significant) increase of this ratio from the Ap (1.7 to 1.9) to the Bw (1.9 to 2.1) and C (2.2 to 2.3) horizons for all three size fractions (Table S6), suggesting increasing proportions of 1:1 clay minerals or Fe/Al (hydr)oxides in the Ap horizon and colloidal silica or quartz in the C horizon. Soil colloids$_{100–450nm}$ seemed to be mainly composed of 2:1 clay minerals due to a molar ratio of around 2.2 (Table S6). The differing associations of P with other elements with respect to the soil horizon followed no clear trend and was partly a combination of clusters from soil colloids$_{0.66–20nm}$ and soil colloids$_{20–100nm}$, indicating the presence of particles from soil colloids$_{0.66–20nm}$ and soil colloids$_{20–100nm}$ in the release peak (soil colloids$_{100–450nm}$).

The clustering between soil colloids$_{0.66–20nm}$ from the C horizon and water colloids$_{20–60nm}$ (Fig. S3) suggests that a large proportion of colloids transported in the water samples may have their origin in the water-extractable nanocolloids within the C horizon. Since the pipes of the tile-drainage system are located in this soil horizon, it is plausible that there is an increased loss of nanocolloids from this horizon. This also agrees with literature attesting that, for the most part, colloids <200 nm are transported below ground (Fresne et al., 2022). Cluster analysis suggested that mainly clay minerals such as illite were transported from the soil into the water through the tile drain, as both soil (soil colloids$_{0.66–20nm}$) and water (water colloids$_{20–60nm}$) exhibited a cluster composed of Al/Fe (soil colloids) or Al (water colloids) and Si. When soil water enters the tile-drain pipes, the redox status and ionic strength of the water are altered (Zimmer et al., 2016). This can not only foster the aggregation of nanocolloidal particles into larger colloids—explaining the larger size of clay particles in the water samples—but can also facilitate the formation of new, e.g., colloidal iron (III) (hydr)oxides and larger particles within the tile drain (i.e., ochre floc formation (Zimmer et al., 2016)). Due to the high P sorption capacity of these particles (Gottselig et al., 2017b), leached truly DP is easily adsorbed to their surface. This is indicated by the clustering of Fe with P in water colloids$_{0.66–20nm}$ from the tile drain, which was not observed in the corresponding size fraction of the soil samples. The fact that Fe and P also clustered in water colloids$_{0.66–20nm}$ and water colloids$_{20–60nm}$ from the ditch implies that this formation and agglomeration of P-bearing colloids proceeded along the flow path with an increasing importance of iron(III) (hydr)oxides over clay particles.

The clustering of soil colloids$_{20–100nm}$ and soil colloids$_{100–450nm}$ from all horizons suggests that colloids are transported within the soil profile. In this context, sorption and desorption processes of colloids during transport and associated aggregation and disintegration processes can influence the size of the colloids and thus their distribution among the size fractions within the horizons. However, in the Ap and Bw horizons, only soil colloids$_{0.66–20nm}$ clustered with colloids in the water samples, which suggests that smaller nanocolloids from the soil are more prone to leaching through the soil profile than fine- and medium-sized soil colloids, as was also found by Fresne et al. (2022). Macropore and preferential flow are the main processes of colloid and particle transport (McGechan and Lewis, 2002; Wang et al., 2020). For instance, Koch et al. (2016) showed that at the present study site, event-based colloidal transport primarily takes place in singular macropores of biogenetic nature, while dissolved forms also pass through the soil matrix, the secondary pore system, or the interaggregate pore space. As a result, the transport of nano-sized colloids to the tile drain via such preferential pathways can be particularly fast, as large parts of the soil matrix get bypassed without substantially affecting the particle size. It is important to note that the results of this study apply only to the period from winter to spring, when vegetation cover is limited and evapotranspiration is minor. As plant water demand and evapotranspiration losses increase during the summer, water flux and P transport will likely vary.

5. Conclusions

In conclusion, our study showed that (i) under baseflow conditions, mainly nano-sized clay-dominated colloids were transported from the soil horizon in which the tile drain was located (C horizon) into adjacent water bodies, while (ii) event flow also enabled the mobilization of larger particles. The fact that the colloidal (<750 nm) fraction was comparable between baseflow and flow events indicates that (iii) the discharge prevailing during the runoff period did not exhaust colloid mobilization and that even under baseflow conditions, colloidal P was exported from the soil through the tile-drainage system. Furthermore, (iv) higher and varying flows during discharge events facilitated the transport of even larger particles (>750 nm) through the soil matrix. The results of this study highlight the role of larger particles and colloids in P export. The impact of rainfall intensity and pattern on particulate P discharge must be considered more closely so that drainage management can be adjusted to achieve reduced P export from agricultural land.

CRediT authorship contribution statement

Nina Siebers: Conceptualization, Data curation, Formal analysis, Funding acquisition, Investigation, Methodology, Project administration,

Validation, Visualization, Writing – original draft, review & editing. **Jens Kruse**: Conceptualization, Data curation, Formal analysis, Investigation, Methodology, Validation, Writing – original draft, review & editing. **Yunsheng Jia**: Data curation, Formal analysis, Investigation, Methodology, Visualization, Writing – original draft, review & editing. **Bernd Lennartz**: Funding acquisition, Project administration, Writing – review & editing. **Stefan Koch**: Conceptualization, Data curation, Formal analysis, Investigation, Methodology, Validation, Writing – review & editing.

Data availability

Data will be made available on request.

Declaration of competing interest

The authors declare that they have no known competing financial interests or personal relationships that could have appeared to influence the work reported in this paper.

Acknowledgments

The authors gratefully acknowledge the funding provided by the German Federal Ministry of Education and Research (BMBF) for the BonaRes project InnoSoilPhos [031B0509D and 031A558] and the technical support provided by P. Narf. Furthermore, we would like to express our deep appreciation for the support of field workers and scientific partners Tilo Hartwig, Evelyn Bolzmann, Petra Kahle, and Andreas Bauwe.

Appendix A. Supplementary data

Supplementary data to this article can be found online at https://doi.org/10.1016/j.scitotenv.2023.161439.

References

Alewell, C., Ringeval, B., Ballabio, C., Robinson, D.A., Panagos, P., Borrelli, P., 2020. Global phosphorus shortage will be aggravated by soil erosion. Nat. Commun. 11, 4546. https://doi.org/10.1038/s41467-020-18326-7.

Andersson, K., Dahlqvist, R., Turner, D., Stolpe, B., Larsson, T., Ingri, J., Andersson, P., 2006. Colloidal rare earth elements in a boreal river: changing sources and distributions during the spring flood. Geochim. Cosmochim. Acta 70, 3261–3274. https://doi.org/10.1016/j.gca.2006.04.021.

Audette, Y., O'Halloran, I.P., Paul Voroney, R., 2016. Kinetics of phosphorus forms applied as inorganic and organic amendments to a calcareous soil. Geoderma 262, 119–124. https://doi.org/10.1016/j.geoderma.2015.08.021.

Baalousha, M., Stolpe, B., Lead, J.R., 2011. Flow field-flow fractionation for the analysis and characterization of natural colloids and manufactured nanoparticles in environmental systems: a critical review. J. Chromatogr. A 1218, 4078–4103.

Bauke, S.L., Amelung, W., Bol, R., Brandt, L., Brüggemann, N., Kandeler, E., Meyer, N., Or, D., Schnepf, A., Schloter, M., Schulz, S., Siebers, N., von Sperber, C., Vereecken, H., 2022. Soil water status shapes nutrient cycling in agroecosystems from micrometer to landscape scales. J. Plant Nutr. Soil Sci. https://doi.org/10.1002/jpln.202200357.

Bender, M.A., dos Santos, D.R., Tiecher, T., Minella, J.P.G., de Barros, C.A.P., Ramon, R., 2018. Phosphorus dynamics during storm events in a subtropical rural catchment in southern Brazil. Agric. Ecosyst. Environ. 261, 93–102. https://doi.org/10.1016/j.agee.2018.04.004.

Bitschofsky, F., Nausch, M., 2019. Spatial and seasonal variations in phosphorus speciation along a river in a lowland catchment (Warnow, Germany). Sci. Total Environ. 657, 671–685. https://doi.org/10.1016/j.scitotenv.2018.12.009.

Burger, D.J., Vogel, J., Kooijman, A.M., Bol, R., de Rijke, E., Schoorl, J., Lücke, A., Gottselig, N., 2021. Colloidal catchment response to snowmelt and precipitation events differs in a forested headwater catchment. Vadose Zone J. 20, e20126. https://doi.org/10.1002/vzj2.20126.

Carpenter, S.R., Bennett, E.M., 2011. Reconsideration of the planetary boundary for phosphorus. Environ. Res. Lett. 6, 014009. https://doi.org/10.1088/1748-9326/6/1/014009.

Chen, A., Arai, Y., 2020. Chapter three - current uncertainties in assessing the colloidal phosphorus loss from soil. In: Sparks, D.L. (Ed.), Advances in Agronomy. Academic Press, pp. 117–151 https://doi.org/10.1016/bs.agron.2020.05.002.

de Jonge, L.W., Moldrup, P., Rubæk, G.H., Schelde, K., Djurhuus, J., 2004. Particle leaching and particle-facilitated transport of phosphorus at field scale. Vadose Zone J. 3, 462–470. https://doi.org/10.2136/vzj2004.0462.

Domagalski, J.L., Johnson, H.M., 2011. Subsurface transport of orthophosphate in five agricultural watersheds,USA. J. Hydrol. 409, 157–171. https://doi.org/10.1016/j.jhydrol.2011.08.014.

Ellerbrock, R.H., Gerke, H.H., 2021. FTIR spectral band shifts explained by OM–cation interactions. J. Plant Nutr. Soil Sci. 184, 388–397. https://doi.org/10.1002/jpln.202100056.

Esbroeck, C.J.V., Macrae, M.L., Brunke, R.R., McKague, K., 2017. Surface and subsurface phosphorus export from agricultural fields during peak flow events over the nongrowing season in regions with cool, temperate climates. J. Soil Water Conserv. 72, 65–76. https://doi.org/10.2489/jswc.72.1.65.

Federal German Government, 2015. Progress Report of the German Strategy for Adaptation to Climate Change. Federal German Government.

Filella, M., Deville, C., Chanudet, V., Vignati, D., 2006. Variability of the colloidal molybdate reactive phosphorous concentrations in freshwaters. Water Res. 40, 3185–3192. https://doi.org/10.1016/j.watres.2006.07.010.

Fresne, M., Jordan, P., Fenton, O., Mellander, P.-E., Daly, K., 2021. Soil chemical and fertilizer influences on soluble and medium-sized colloidal phosphorus in agricultural soils. Sci. Total Environ. 754, 142112. https://doi.org/10.1016/j.scitotenv.2020.142112.

Fresne, M., Jordan, P., Daly, K., Fenton, O., Mellander, P.-E., 2022. The role of colloids and other fractions in the below-ground delivery of phosphorus from agricultural hillslopes to streams. Catena 208, 105735. https://doi.org/10.1016/j.catena.2021.105735.

Gerke, J., 2010. Humic (organic matter)-Al(Fe)-phosphate complexes: an underestimated phosphate form in soils and source of plant-available phosphate. Soil Sci. 175, 417–425. https://doi.org/10.1097/SS.0b013e3181f1b4dd.

German Environment Agency, 2019. Monitoring Report on the German Strategy for Adaptation to Climate Change.

Gottselig, N., Bol, R., Nischwitz, V., Vereecken, H., Amelung, W., Klumpp, E., 2014. Distribution of phosphorus-containing fine colloids and nanoparticles in stream water of a forest catchment. Vadose Zone J. 13, vzj2014.01.0005. https://doi.org/10.2136/vzj2014.01.0005.

Gottselig, N., Amelung, W., Kirchner, J.W., Bol, R., Eugster, W., Granger, S.J., Hernández-Crespo, C., Herrmann, F., Keizer, J.J., Korkiakoski, M., Laudon, H., Lehner, I., Löfgren, S., Lohila, A., Macleod, C.J.A., Mölder, M., Müller, C., Nasta, P., Nischwitz, V., Paul-Limoges, E., Pierret, M.C., Pilegaard, K., Romano, N., Sebastià, M.T., Stähli, M., Voltz, M., Vereecken, H., Siemens, J., Klumpp, E., 2017a. Elemental composition of natural nanoparticles and fine colloids in European forest stream waters and their role as phosphorus carriers. Glob. Biogeochem. Cycles 31, 1592–1607. https://doi.org/10.1002/2017GB005657.

Gottselig, N., Nischwitz, V., Meyn, T., Amelung, W., Bol, R., Hallé, C., Vereecken, H., Siemens, J., Klumpp, E., 2017b. Phosphorus binding to nanoparticles and colloids in forest stream waters. Vadose Zone J. 16. https://doi.org/10.2136/vzj2016.07.0064.

Greenberg, A.E., Rhodes, T.R., Clesceri, L., 1985. Standard Methods for the Examination of Water and Wastewater. 16th ed. .

Gu, S., 2017. Release of Dissolved and Colloidal Phosphorus From Riparian Wetlands: A Field and Laboratory Assessment of the Mechanisms and Controlling Factors. Université Rennes 1 (phdthesis).

Gu, S., Gruau, G., Dupas, R., Jeanneau, L., 2020. Evidence of colloids as important phosphorus carriers in natural soil and stream waters in an agricultural catchment. J. Environ. Qual. 49, 921–932. https://doi.org/10.1002/jeq2.20090.

Hahn, C., Prasuhn, V., Stamm, C., Milledge, D.G., Schulin, R., 2014. A comparison of three simple approaches to identify critical areas for runoff and dissolved reactive phosphorus losses. Hydrol. Earth Syst. Sci. 18, 2975–2991. https://doi.org/10.5194/hess-18-2975-2014.

Hamer, M., Graham, R.C., Amrhein, C., Bozhilov, K.N., 2003. Dissolution of ripidolite (Mg, Fe-chlorite) in organic and inorganic acid solutions. Soil Sci. Soc. Am. J. 67, 654–661. https://doi.org/10.2136/sssaj2003.6540.

Hassellöv, M., von der Kammer, F., 2008. Iron oxides as geochemical nanovectors for metal transport in soil-river systems. Elements 4, 401–406. https://doi.org/10.2113/gselements.4.6.401.

HELCOM, 2018. HELCOM Thematic assessment of eutrophication 2011-2016. Baltic Sea Environment Proceedings No. 156.

HELCOM, 2018. Sources and pathways of nutrients to the Baltic Sea. Baltic Sea Environment Proceedings No. 153.

HELCOM, 2022. Inputs of nutrients to the sub-basins (2019). HELCOM core indicator report. Online. [29.10.22] https://helcom.fi/wp-content/uploads/2017/06/HELCOM-core-indicator-on-inputs-of-nutrients-for-period-1995-2019.pdf.

Helfenstein, J., Tamburini, F., von Sperber, C., Massey, M.S., Pistocchi, C., Chadwick, O.A., Vitousek, P.M., Kretzschmar, R., Frossard, E., 2018. Combining spectroscopic and isotopic techniques gives a dynamic view of phosphorus cycling in soil. Nat. Commun. 9, 3226. https://doi.org/10.1038/s41467-018-05731-2.

Henderson, R., Kabengi, N., Mantripragada, N., Cabrera, M., Hassan, S., Thompson, A., 2012. Anoxia-induced release of colloid-and nanoparticle-bound phosphorus in grassland soils. Environ. Sci. Technol. 46, 11727–11734.

Hens, M., Merckx, R., 2002. The role of colloidal particles in the speciation and analysis of "dissolved" phosphorus. Water Res. 36, 1483–1492. https://doi.org/10.1016/s0043-1354(01)00349-9.

Jarvie, H.P., Neal, C., Rowland, A.P., Neal, M., Morris, P.N., Lead, J.R., Lawlor, A.J., Woods, C., Vincent, C., Guyatt, H., Hockenhull, K., 2012. Role of riverine colloids in macronutrient and metal partitioning and transport, along an upland-lowland land-use continuum, under low-flow conditions. Sci. Total Environ. 434, 171–185. https://doi.org/10.1016/j.scitotenv.2011.11.061.

Jiang, X., Bol, R., Nischwitz, V., Siebers, N., Willbold, S., Vereecken, H., Amelung, W., Klumpp, E., 2015. Phosphorus containing water dispersible nanoparticles in arable soil. J. Environ. Qual. 44, 1772–1781. https://doi.org/10.2134/jeq2015.02.0085.

Jiang, X., Livi, K.J.T., Arenberg, M.R., Chen, A., Chen, K.-Y., Gentry, L., Li, Z., Xu, S., Arai, Y., 2021. High flow event induced the subsurface transport of particulate phosphorus and its speciation in agricultural tile drainage system. Chemosphere 263, 128147. https://doi.org/10.1016/j.chemosphere.2020.128147.

Jordan-Meille, L., Dorioz, J.M., 2004. Soluble phosphorus dynamics in an agricultural watershed. Agronomie 24, 237–248. https://doi.org/10.1051/agro:2004021.

Kahle, P., 2009. Methodische Aspekte zum Monitoring der Wasserqualität künstlich entwässerter Tieflandeinzugsgebiete = Methodological aspects of water-quality monitoring in artificially drained lowland catchment. Hydrol. Wasserbewirtsch. 53, 228.

Kjaergaard, C., Moldrup, P., de Jonge, L.W., Jacobsen, O.H., 2004. Colloid mobilization and transport in undisturbed soil columns. II. The role of colloid dispersibility and preferential flow. Vadose Zone J. 3, 424–433. https://doi.org/10.2136/vzj2004.0424.

Kleinman, P.J.A., Allen, A.L., Needelman, B.A., Sharpley, A.N., Vadas, P.A., Saporito, L.S., Folmar, G.J., Bryant, R.B., 2007. Dynamics of phosphorus transfers from heavily manured Coastal Plain soils to drainage ditches. J. Soil Water Conserv. 62, 225–235.

Koch, S., Kahle, P., Lennartz, B., 2016. Visualization of colloid transport pathways in mineral soils using Titanium(IV) oxide as a tracer. J. Environ. Qual. 45, 2053–2059. https://doi.org/10.2134/jeq2016.04.0131.

Koch, S., Kahle, P., Lennartz, B., 2019. Biogas digestate application modifies solute transport conditions in soils and increases the release of phosphorus. Vadose Zone J. 18. https://doi.org/10.2136/vzj2019.03.0031.

Koroleff, J., 1983. Determination of total phosphorus by alkaline persulphate oxidation. Methods Seawater Anal. Verl. Chem. Wienheim, pp. 136–138.

Krause, L., Klumpp, E., Nofz, I., Missong, A., Amelung, W., Siebers, N., 2020. Colloidal iron and organic carbon control soil aggregate formation and stability in arable luvisols. Geoderma 374, 114421. https://doi.org/10.1016/j.geoderma.2020.114421.

Liu, J., Yang, J., Liang, X., Zhao, Y., Cade-Menun, B.J., Hu, Y., 2014. Molecular speciation of phosphorus present in readily dispersible colloids from agricultural soils. Soil Sci. Soc. Am. J. 78, 47–53. https://doi.org/10.2136/sssaj2013.05.0159.

Lyne, V., Hollick, M., 1979. Stochastic time-variable rainfall-runoff modelling. Institute of Engineers Australia National Conference. Institute of Engineers Australia Barton, Australia, pp. 89–93.

McGechan, M.B., Lewis, D.R., 2002. SW—soil and water: transport of particulate and colloid-sorbed contaminants through soil, part 1: general principles. Biosyst. Eng. 83, 255–273. https://doi.org/10.1006/bioe.2002.0125.

Missong, A., Holzmann, S., Bol, R., Nischwitz, V., Puhlmann, H., v. Wilpert, K., Siemens, J., Klumpp, E., 2018. Leaching of natural colloids from forest topsoils and their relevance for phosphorus mobility. Sci. Total Environ. 634, 305–315. https://doi.org/10.1016/j.scitotenv.2018.03.265.

Nathan, R.J., McMahon, T.A., 1990. Evaluation of automated techniques for base flow and recession analyses. Water Resour. Res. 26, 1465–1473. https://doi.org/10.1029/WR026i007p01465.

Nausch, G., 2011. Eutrophierung der Ostsee. Meeresverschmutzung und Meeresschutz. Chem. Unserer Zeit. 45, pp. 164–170. https://doi.org/10.1002/ciuz.201100537.

Nausch, M., Woelk, J., Kahle, P., Nausch, G., Leipe, T., Lennartz, B., 2017. Phosphorus fractions in discharges from artificially drained lowland catchments (Warnow River, Baltic Sea). Agric. Water Manag. 187, 77–87.

Nazari, S., Ford, W.I., King, K.W., 2022. Impact of flow pathway and source water connectivity on subsurface sediment and particulate phosphorus dynamics in tile-drained agroecosystems. Agric. Water Manag. 269, 107641. https://doi.org/10.1016/j.agwat.2022.107641.

Neubauer, E., von der Kammer, F., Hofmann, T., 2013. Using FLOWFFF and HPSEC to determine trace metal colloid associations in wetland runoff. Water Res. 47. https://doi.org/10.1016/j.watres.2013.02.030.

Nischwitz, V., Gottselig, N., Missong, A., Meyn, T., Klumpp, E., 2016. Field flow fractionation online with ICP-MS as novel approach for the quantification of fine particulate carbon in stream water samples and soil extracts. J. Anal. At. Spectrom. 31, 1858–1868. https://doi.org/10.1039/C6JA00027D.

Quinton, J.N., Govers, G., Van Oost, K., Bardgett, R.D., 2010. The impact of agricultural soil erosion on biogeochemical cycling. Nat. Geosci. 3, 311–314. https://doi.org/10.1038/ngeo838.

Qureshi, R.N., Kok, W.T., 2011. Application of flow field-flow fractionation for the characterization of macromolecules of biological interest: a review. Anal. Bioanal. Chem. 399, 1401–1411.

Rodriguez, J.A., Lustosa Filho, J.F., Melo, L.C.A., de Assis, I.R., de Oliveira, T.S., 2020. Influence of pyrolysis temperature and feedstock on the properties of biochars produced from agricultural and industrial wastes. J. Anal. Appl. Pyrolysis 149, 104839. https://doi.org/10.1016/j.jaap.2020.104839.

Rowley, M.C., Grand, S., Verrecchia, É.P., 2018. Calcium-mediated stabilisation of soil organic carbon. Biogeochemistry 137, 27–49. https://doi.org/10.1007/s10533-017-0410-1.

Ruark, M., Madison, A., Cooley, E., Stuntebeck, T., Komiskey, M., 2012. Phosphorus loss form tile drains: should we be concerned? Proc. 2012 Wis. Crop Manag. Conf. 51

Rubæk, G.H., Kristensen, K., Olesen, S.E., Østergaard, H.S., Heckrath, G., 2013. Phosphorus accumulation and spatial distribution in agricultural soils in Denmark. Geoderma 209, 241–250.

Schelde, K., Moldrup, P., Jacobsen, O.H., de Jonge, H., de Jonge, L.W., Komatsu, T., 2002. Diffusion-limited mobilization and transport of natural colloids in macroporous soil. Vadose Zone J. 1, 125–136. https://doi.org/10.2136/vzj2002.1250.

Schimpf, M.E., Caldwell, K., Giddings, J.C., 2000. Retention normal mode. Field-Flow Fractionation Handb. 31.

Tiemeyer, B., Kahle, P., Lennartz, B., 2006. Nutrient losses from artificially drained catchments in North-Eastern Germany at different scales. Agric. Water Manag. 85, 47–57. https://doi.org/10.1016/j.agwat.2006.03.016.

Tiemeyer, B., Kahle, P., Lennartz, B., 2009. Phosphorus losses from an artificially drained rural lowland catchment in North-Eastern Germany. Agric. Water Manag. Int. J. 96, 677–690. https://doi.org/10.1016/j.agwat.2008.10.004.

Totsche, K.U., Amelung, W., Gerzabek, M.H., Guggenberger, G., Klumpp, E., Knief, C., Lehndorff, E., Mikutta, R., Peth, S., Prechtel, A., Ray, N., Kögel-Knabner, I., 2018. Microaggregates in soils. J. Plant Nutr. Soil Sci. 181, 104–136. https://doi.org/10.1002/jpln.201600451.

Wang, C., Wang, R., Huo, Z., Xie, E., Dahlke, H.E., 2020. Colloid transport through soil and other porous media under transient flow conditions—a review. WIREs Water 7, e1439. https://doi.org/10.1002/wat2.1439.

WRB, I., 2007. Working Group (2006) World reference base for soil resources 2006. World Soil Res. Rep. (103).

Yaghi, N., Hartikainen, H., 2013. Enhancement of phosphorus sorption onto light expanded clay aggregates by means of aluminum and iron oxide coatings. Chemosphere 93, 1879–1886. https://doi.org/10.1016/j.chemosphere.2013.06.059.

Zhuang, J., McCarthy, J.F., Tyner, J.S., Perfect, E., Flury, M., 2007. In situ colloid mobilization in Hanford sediments under unsaturated transient flow conditions: effect of irrigation pattern. Environ. Sci. Technol. 41, 3199–3204. https://doi.org/10.1021/es062757h.

Zimmer, D., Kahle, P., Baum, C., 2016. Loss of soil phosphorus by tile drains during storm events. Agric. Water Manag. 167, 21–28. https://doi.org/10.1016/j.agwat.2015.12.017.